Journal of Photochemistry & Photobiology, A: Chemistry 469 (2025) 116573

Contents lists available at ScienceDirect

Journal of Photochemistry & Photobiology, A: Chemistry

journal homepage: www.elsevier.com/locate/jphotochem

Ring strain integrity in the absorption spectrum of β-propiolactone: VUV spectroscopy in the photon energy 4.6–10.8 eV

P.A.S. Randi [a], M.H.F. Bettega [a,*], N.C. Jones [b], S.V. Hoffmann [b], L. Zuin [c], M. Macdonald [c], N.J. Mason [d], M.A. Śmiałek [e,*], P. Limão-Vieira [a,f,**]

[a] Departamento de Física, Universidade Federal do Paraná, Caixa Postal 19044, 81531-980 Curitiba, Paraná, Brazil
[b] ISA, Department of Physics and Astronomy, Aarhus University, Ny Munkegade 120, DK-8000 Aarhus C, Denmark
[c] Canadian Light Source Inc., 44 Innovation Boulevard, Saskatoon S7N 2V3, Canada
[d] Physics and Astronomy, University of Kent, Canterbury CT2 7NH, United Kingdom
[e] Faculty of Mechanical Engineering and Ship Technology, Institute of Naval Architecture, Gdansk University of Technology, Narutowicza 11/12, 80-233 Gdansk, Poland
[f] Atomic and Molecular Collisions Laboratory, CEFITEC, Department of Physics, NOVA School of Science and Technology, Universidade NOVA de Lisboa, 2829-516 Caparica, Portugal

ARTICLE INFO

Keywords:
β-Propiolactone
Ultraviolet radiation
Cross-sections
Theoretical calculations
Ring strain integrity

ABSTRACT

New absolute cross-section values are reported from high-resolution vacuum ultraviolet (VUV) photoabsorption measurements of β-propiolactone in the photon energy range 4.6–10.8 eV (268–115 nm). The assignment of the different vibronic features has been performed with the aid of quantum chemical calculations that provide vertical energies, oscillator strengths and harmonic frequencies. The joint experimental and theoretical methodology employed provides a comprehensive review of the electronic state spectroscopy of $CH_2CH_2CO_2$. A photoelectron spectrum has also been recorded from 10 up to 24 eV and compared to earlier data in the literature. A new value of (10.560 ± 0.002) eV for the ground ionic state adiabatic ionisation energy is recommended. The vibrational features in the spectral bands are assigned to C=O stretching, $\nu'_3(a')$, CH_2 wagging, $\nu'_6(a')$, ring C–O stretching, $\nu'_{10}(a')$, and C=O in-plane bending, $\nu'_{13}(a')$ modes. Potential energy curves for the lowest-lying electronic excited states, as a function of the C–O/C=O coordinates, have been obtained from time-dependent density functional theory (TD-DFT). Ring strain integrity is shown to be a fragile mechanism upon electronic excitation. The calculations have also shed light on the relevant internal conversion from the electronic excited states governing the nuclear dynamics with significant pre-dissociative character of the lowest-lying electronic states.

1. Introduction

Beta-propiolactone (β-propiolactone), $CH_2CH_2CO_2$, is a commercially relevant chemical compound that has been widely used in the organic synthesis of acrylic acid and esters, used in the plastics and solvent industry. However, it is also considered a potential human carcinogen agent [1–5] (and references therein). Different investigations, including experimental and theoretical methodologies, have been performed to assess the role of $CH_2CH_2CO_2$ with purine nucleosides of nucleic acids showing that carcinogenesis is related to the lactone's reactivity [4,6]; other studies concern the role of low-concentration β-propiolactone in inactivating the human influenza virus [6]. Currently it is still used in vaccine production for the inactivation of viruses [1,6,7], however its general use has decreased significantly [2].

Once released into the atmosphere, gas-phase β-propiolactone can undergo a degradation process with $^{\bullet}OH$ radicals with an estimated half-life of 45 days [2], while the thermal stability of β-lactones has been reported with the main aim to address ring strain and even ring opening mechanisms [8]. Notwithstanding these works, we note that a comprehensive description of β-propiolactone electronic state spectroscopy (valence and Rydberg excitations) in the vacuum ultraviolet

* Corresponding authors.
** Corresponding author at: Departamento de Física, Universidade Federal do Paraná, Caixa Postal 19044, 81531-980 Curitiba, Paraná, Brazil; CEFITEC, Department of Physics, NOVA School of Science and Technology, Universidade NOVA de Lisboa, 2829-516 Caparica, Portugal.
E-mail addresses: bettega@fisica.ufpr.br (M.H.F. Bettega), smialek@pg.edu.pl (M.A. Śmiałek), plimaovieira@fct.unl.pt (P. Limão-Vieira).

https://doi.org/10.1016/j.jphotochem.2025.116573
Received 14 April 2025; Received in revised form 3 June 2025; Accepted 10 June 2025
Available online 11 June 2025

(VUV) photon energy region is lacking. Such information combined with other spectroscopic techniques is fundamental to a detailed knowledge of the electronic and molecular structures of this chemical compound regarding its chemical stability.

A thorough literature survey reveals only a few experimental investigations with infrared and Raman spectroscopies [3,5,9,10], and measurement of the lowest-lying ionic states by He(I) photoelectron and photoionisation spectroscopies [11–13]. Also relevant are *ab initio* methods used on the electronic and molecular structure [8] and vibrational spectra calculations [10].

The combined experimental and theoretical studies reported in this paper provide, for the first time, a detailed characterisation of β-propiolactone lowest-lying neutral electronic states over the photon energy (wavelength) range 5.0–10.8 eV (248–115 nm), while the ionic electronic states have been probed from 10 up to 24 eV (124–52 nm). Complementary time-dependent density functional theory (TD-DFT/CAM-B3LYP/aug-cc-pVTZ) and Equation-of-Motion Coupled-Cluster Singles and Doubles (EOM-CCSD/aug-cc-pVTZ) calculations provide vertical excitation energies and oscillator strengths for the neutral excited states. Additionally, the geometries and vibrational frequencies of the neutral, first excited neutral and cationic ground-state, and potential energy curves for the lowest-lying excited states are obtained using the TD-DFT method.

The structure of this paper includes Section 2 with a brief description of the experimental methods, while Section 3 is devoted to the theoretical methodology. Section 4 reports the structure and properties of β-propiolactone. Section 5 presents the results and discussion, including a detailed description of the major electronic excitations and the assignments of the fine structure in the VUV spectrum, together with the ionisation energies obtained from the photoelectron spectroscopy and the assignment of the different Rydberg states. We conclude in Section 6 with an overall analysis of the electronic state spectroscopy of β-propiolactone, $CH_2CH_2CO_2$.

2. Experimental methods

2.1. VUV photoabsorption

The AU-UV beam line of the ASTRID2 synchrotron facility at Aarhus University, Denmark was used to obtain absolute cross-section values of β-propiolactone. The high-resolution vacuum ultraviolet (VUV) photoabsorption spectrum measured in the photon energy (wavelength) range from 4.63–10.781 eV (268–115 nm) is shown in Fig. 1 with expanded sections in Figs. 2–5, while assignments of the different absorption features are shown in Tables 1–6. The experimental setup has been described elsewhere [14,15], so only a brief description is given here.

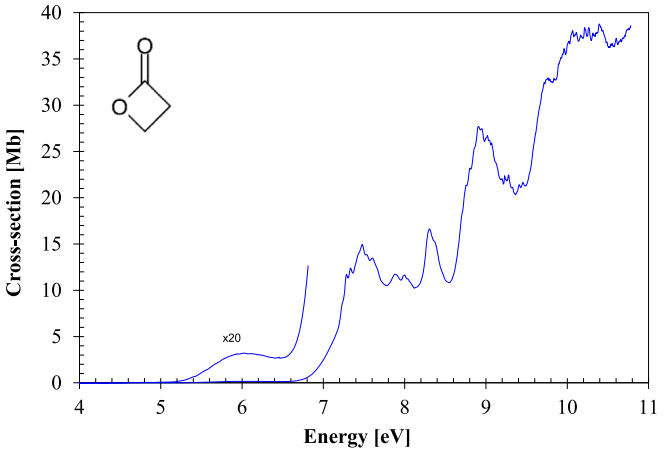

Fig. 1. High-resolution VUV photoabsorption spectrum of $CH_2CH_2CO_2$ in the 4.0–10.8 eV photon energy range. See text for details.

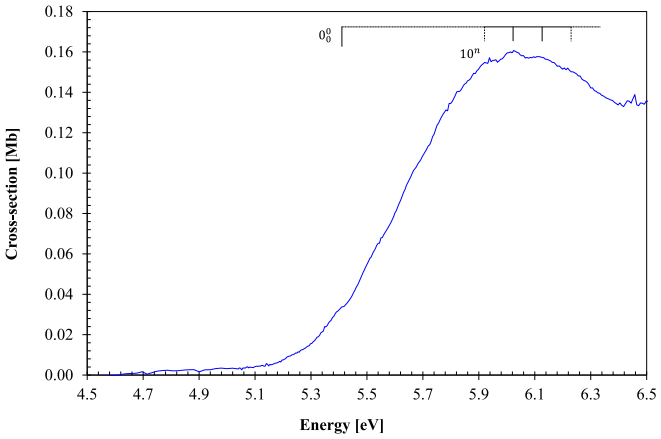

Fig. 2. Details of the VUV photoabsorption spectrum of $CH_2CH_2CO_2$ in the 4.5–6.5 eV photon energy range. See text for details.

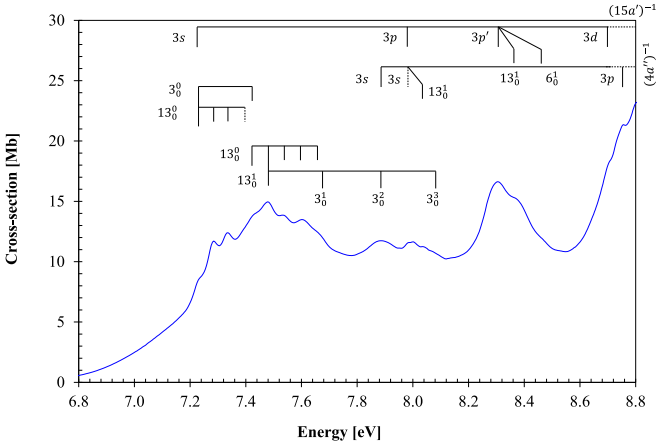

Fig. 3. Details of the VUV photoabsorption spectrum of CH_2 CH_2 CO_2 in the 6.8–8.8 eV photon energy range. See text for details.

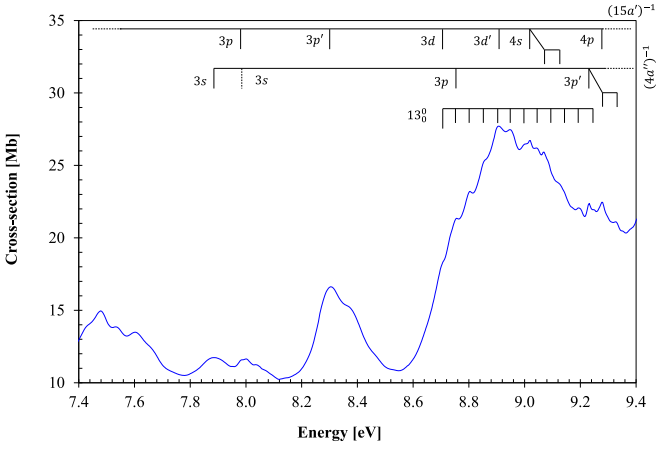

Fig. 4. Detail of the VUV photoabsorption spectrum of $CH_2CH_2CO_2$ in the 7.4–9.4 eV photon energy range. See text for details.

Synchrotron radiation passes through a static gas sample filled with β-propiolactone vapour at room temperature. The transmission windows (MgF_2) set the lower wavelength limit of detection (115 nm) with transmitted light detected by a photomultiplier tube (PMT). A capacitance manometer (Chell CDG100D) was used to measure the absolute pressure of the sample in the absorption cell. The absorption cross-

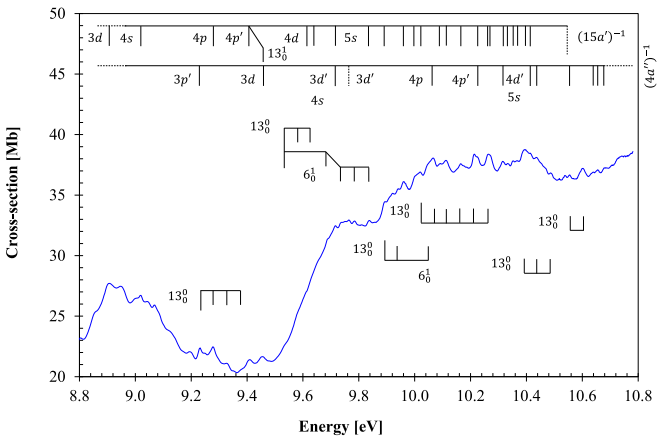

Fig. 5. Detail of the VUV photoabsorption spectrum of $CH_2CH_2CO_2$ in the 9.0–10.8 eV photon energy range. See text for details.

sections were measured in the pressure range 0.09–1.21 mbar, as appropriate for the local cross-section, to achieve attenuations of 50 % or less and hence avoid saturation effects.

The absolute photoabsorption cross-sections values, σ, in units of megabarn (1 Mb $\equiv 10^{-18}$ cm^2) were obtained using the Beer-Lambert attenuation law, $I_t = I_0 e^{(-N\sigma l)}$, where I_t is the light intensity transmitted through the gas sample, I_0 is that through the evacuated cell, N is the molecular number density of $CH_2CH_2CO_2$, and l the absorption path length (15.5 cm). Throughout the collection of each spectrum, the synchrotron beam current was monitored, and background scans, I_0, were recorded with the cell evacuated. ASTRID2 operates in a "top-up" mode allowing the light intensity to be kept quasi-constant, thus compensating for the constant beam decay in the storage ring. The variations (2–3 %) of the incident flux are therefore normalized to the beam current in the storage ring. Following the methodology employed, within the wavelength region scanned (115–310 nm), accurate cross-section values are obtained by recording the VUV spectrum in small (5 or 10 nm) sections, allowing an overlap of at least 10 data points between the adjoining sections and optimising the pressure used according to the cross-section of the features. This methodology allows us to determine photoabsorption cross-sections to an accuracy of ± 5 %. The resolution in the present spectrum [14] is 0.08 nm (corresponding to 1, 3, and 7 meV at the low extreme, the midpoint, and the high extreme of the present energy range, respectively).

The liquid sample used in the VUV photoabsorption measurements was purchased from Sigma-Aldrich, with a stated purity of 97 %. The sample was degassed through repeated freeze–pump–thaw cycles.

2.2. Threshold photoelectron spectroscopy

The threshold photoelectron spectrum of β-propiolactone is shown in Fig. 6 with assignments of the fine structure in Table 5 based on the calculated harmonic frequencies for the cation electronic ground-state (see supporting material).

Photoelectron and threshold photoelectron spectra were obtained at the VLSPGM beamline [16] at the Canadian Light Source facility in Saskatoon, Canada. The measurements were conducted using a double toroidal coincidence spectrometer, originally designed for analysing noble gases and small diatomic molecules [17]. Recently, it has been shown that this spectrometer can also be utilized for studying more complex systems [18]. In our experiments we have used the data collected by the 180° toroidal detector, set at a pass energy of 4 eV. The photoexcitation energy of the photoelectron spectrum presented here was 80 eV, recorded with the entrance and exit slits of the VLS-PGM beamline set to 50 μm due to higher photon flux than at 70 eV. The spectrum presented here was calibrated against the $\tilde{X}^2\sum_g^+$, $\nu' = 0$ and $\tilde{A}^2\Pi_u$ $\nu' = 0$ peaks of N_2^+, rounded to three decimal places [19,20]. The measured resolution from the nitrogen calibration spectrum was 60 meV.

The liquid sample used in the PES measurements was purchased from Sigma-Aldrich, with a stated purity of 97 %. The sample was degassed through repeated freeze–pump–thaw cycles.

3. Theoretical methods

The optimised neutral ground, neutral first excited and cationic ground state geometries have been obtained from DFT/CAM-B3LYP/aug-cc-pVTZ and TD-DFT/CAM-B3LYP/aug-cc-pVTZ calculations [21] in the GAMESS-US computational package [22]. Their bond lengths in Å and bond angles in (°) are shown in Figs. S1–S3. The VUV photoabsorption features in Fig. 1 have been assigned with the aid of the TD-DFT method [23,24] with a CAM-B3LYP functional [21], and the aug-cc-pVTZ basis set, thus providing vertical excitation energies and oscillator strengths of the electronically excited states of β-propiolactone (see Table 1). In the supplementary material we include Table S1 with a complete set of the electronic transitions and oscillator strengths. The aug-cc-pVTZ set ensures a reliable description of the electronic structure, particularly for transitions involving highly delocalized orbitals, such as in Rydberg and mixed valence-Rydberg states. CAM-B3LYP was chosen for its long-range corrected hybrid functional approach, which is particularly suitable for polar molecules. Other functionals and basis sets were tested (not shown here), but the CAM-B3LYP/aug-cc-pVTZ combination provided the best agreement with experimental data, making it the most reliable choice for accurately describing the electronic excitations of the system. Additional calculations have been

Table 1
The calculated vertical excitation energies (TD-DFT/CAM-B3LYP/aug-cc-pVTZ) and oscillator strengths of the $CH_2CH_2CO_2$ compared with the present experimental data. Energies in eV. See text for details.

β-propiolactone				E (eV) expt.[a]	Cross-section (Mb)
State	E (eV)	f_L	Dominant excitations		
$\tilde{X}$ ^{1}A′					
1 ^{1}A″	6.050	0.000594	$\pi^*_{CO}/3d'(6a'')\leftarrow\bar{n}_O/\sigma_{CC}(15a')$(30 %), $\pi^*_{CO}(7a'')\leftarrow\bar{n}_O/\sigma_{CC}(15a')$ (57 %)	6.02(5)	0.16
2 ^{1}A′	7.403	0.034114	$3s(16a')\leftarrow\bar{n}_O/\sigma_{CC}(15a')$(71 %), $\sigma^*_{CC}/3p''(18a')\leftarrow\bar{n}_O/\sigma_{CC}(15a')$ (13 %)	7.341	12.32
3 ^{1}A′	7.959	0.028957	$\pi^*_{CO}/3p(5a'')\leftarrow n_O(4a'')$(15 %), $\sigma^*_{CC}/3p''(18a')\leftarrow\bar{n}_O/\sigma_{CC}(15a')$ (22 %), $\pi^*_{CO}(7a'')\leftarrow n_O(4a'')$ (46 %)	7.487	14.82
5 ^{1}A′	8.391	0.037936	$\pi^*_{CO}/3p(5a'')\leftarrow n_O(4a'')$(23 %), $3p'(17a')\leftarrow\bar{n}_O/\sigma_{CC}(15a')$ (23 %), $\sigma^*_{CC}/3p''(18a')\leftarrow\bar{n}_O/\sigma_{CC}(15a')$ (37 %)	7.890/7.989	11.73/11.59
6 ^{1}A′	8.763	0.059082	$\pi^*_{CO}/3p(5a'')\leftarrow n_O(4a'')$(48 %), $\pi^*_{CO}/3d'(6a'')\leftarrow n_O(4a'')$ (15 %), $\pi^*_{CO}(7a'')\leftarrow n_O(4a'')$ (13 %)	8.316	16.48
7 ^{1}A′	9.021	0.069756	$\sigma^*_{CO}/3d(20a')\leftarrow\bar{n}_O/\sigma_{CC}(15a')$(57 %), $3d'(21a')\leftarrow\bar{n}_O/\sigma_{CC}(15a')$ (21 %)	8.907	27.71
10 ^{1}A′	9.407	0.029759	$\sigma^*_{CO}/3d(20a')\leftarrow\bar{n}_O/\sigma_{CC}(15a')$(11 %), $3d'(21a')\leftarrow\bar{n}_O/\sigma_{CC}(15a')$ (60 %)	9.277	22.46
16 ^{1}A′	10.142	0.064265	$\pi^*_{CO}(7a'')\leftarrow\pi_{CO}(14a')$(53 %), $\sigma^*_{CC}/4s(23a')\leftarrow\bar{n}_O/\sigma_{CC}(15a')$ (15 %)	9.764	32.95
19 ^{1}A′	10.590	0.046692	$\sigma^*_{CO}/3d''(22a')\leftarrow\bar{n}_O/\sigma_{CC}(15a')$(13 %), $\sigma^*_{CO}/3d''(24a')\leftarrow\bar{n}_O/\sigma_{CC}(15a')$ (14 %), $\sigma^*_{CO}/3d(25a')\leftarrow\bar{n}_O/\sigma_{CC}(15a')$ (18 %)	10.394	38.76

[a] The last decimal of the energy value is given in brackets for these less-resolved features;

Table 2
Proposed vibrational assignments of CH_2 CH_2 CO_2 absorption band in the photon energy range 4.5 − 8.6 eV[a]. Energies in eV. See text for details.

This work					
assignment	energy	$\Delta E(\nu'_3)$	$\Delta E(\nu'_6)$	$\Delta E(\nu'_{10})$	$\Delta E(\nu'_{13})$
$\pi^*_{CO}(7a'')\leftarrow\overline{n}_O/\sigma_{CC}(15a') + \pi^*_{CO}/3d'(6a'')\leftarrow\overline{n}_O/\sigma_{CC}(15a'), (1\,^1A''\leftarrow\widetilde{X}^1A')$					
0^0_0	5.40(9)(s)	–	–	–	–
–	…	–	–	–	–
10^n	5.92(1)(s,b)	–	–	–	–
10^{n+1}	6.03(0)(b)	–	–	0.109	–
10^{n+2}	6.12(6)(s,b)	–	–	0.096	–
10^{n+3}	6.22(4)(s,w)	–	–	0.098	–
$3s(16a') + \sigma^*_{CC}/3p''(18a')\leftarrow\overline{n}_O/\sigma_{CC}(15a'), (2\,^1A'\leftarrow\widetilde{X}^1A')$					
$3s(15a')^{-1}$	7.23(8)(s)	–	–	–	–
13^1_0	7.289	–	–	–	0.051
13^2_0	7.341	–	–	–	0.052
3^1_0	7.44(2)(s,w)	0.204	–	–	–
$\sigma^*_{CC}/3p''(18a')\leftarrow\overline{n}_O/\sigma_{CC}(15a') + (\pi^*_{CO}/3p(5a'')+\pi^*_{CO}(7a'')\leftarrow n_O(4a'')), (3\,^1A'\leftarrow\widetilde{X}^1A')$					
0^0_0	7.44(2)(s,w)	–	–	–	–
13^1_0	7.487	–	–	–	0.045
13^2_0	7.533	–	–	–	0.046
13^3_0	7.597	–	–	–	0.064
13^4_0	7.65(8)(s)	–	–	–	0.061
$13^1_03^1_0$	7.68(2)(s)	0.195	–	–	–
$13^1_03^2_0/3s(4a'')^{-1}$	7.89(0)(b)	0.208	–	–	–
$13^1_03^3_0/3s(4a'')^{-1}3^1_0$	8.08(2)(s)	0.192	–	–	–
$\pi^*_{CO}/3p(5a'')\leftarrow n_O(4a'') + (3p'(17a')+\sigma^*_{CC}/3p''(18a'))\leftarrow\overline{n}_O/\sigma_{CC}(15a'), (5\,^1A'\leftarrow\widetilde{X}^1A')$					
$3s(4a'')^{-1}/3p(15a')^{-1}$	7.989	–	–	–	–
13^1_0	8.048	–	–	–	0.059
$(\pi^*_{CO}/3p(5a'')+\pi^*_{CO}/3d'(6a'')+\pi^*_{CO}(7a'')\leftarrow n_O(4a'')), (5\,^1A'\leftarrow\widetilde{X}^1A')$					
$3p'(15a')^{-1}$	8.316	–	–	–	–
13^1_0	8.37(5)(s)	–	–	–	0.059
6^1_0	8.46(9)(s)	–	0.153	–	–
	$\overline{\Delta E}$	0.200	0.153	0.101	0.055

[a] (s) shoulder structure; (w) weak feature; (b) broad feature (the last decimal of the energy value is given in brackets for these less-resolved features);

Table 3
Proposed vibrational assignments of $CH_2CH_2CO_2$ absorption band in the photon energy range 8.6 − 9.4 eV[a]. Energies in eV. See text for details.

This work				
assignment	energy	$\Delta E(\nu'_3)$	$\Delta E(\nu'_6)$	$\Delta E(\nu'_{13})$
$\sigma^*_{CO}/3d(20a') + 3d'(21a')\leftarrow\overline{n}_O/\sigma_{CC}(15a'), \left(7\,^1A'\leftarrow\widetilde{X}^1A'\right)$				
$3d(15a')^{-1}$	8.707	–	–	–
13^1_0	8.762	–	–	0.055
13^2_0	8.803	–	–	0.041
$13^3_0/6^1_0$	8.85(3)(s)		0.146	0.050
$13^4_0/3d'(15a')^{-1}/3^1_0$	8.907	0.200	–	0.054
$13^5_0/3d'(15a')^{-1}3^1_0$	8.952	–	–	0.045
$13^6_0/6^2_0/3d'(15a')^{-1}3^2_0$	9.00(4)(s)	–	0.151	0.052
$13^7_0/3d'(15a')^{-1}3^3_0$	9.04(7)(s)	–	–	0.043
$13^8_0/3^2_0/3d'(15a')^{-1}3^4_0$	9.09(6)(s)	0.189	–	0.049
$13^9_0/6^3_0/3d'(15a')^{-1}3^5_0$	9.14(7)(s)	–	0.143	0.051
$13^{10}_0/3d'(15a')^{-1}3^6_0$	9.201	–	–	0.054
$13^{11}_0/3d'(15a')^{-1}3^7_0$	9.25(6)(w)	–	–	0.055
$4s(15a')^{-1}$	9.020	–	–	–
13^1_0	9.070			0.050
13^2_0	9.12(3)(s)	–	–	0.053
$\sigma^*_{CO}/3d(20a') + 3d'(21a')\leftarrow\overline{n}_O/\sigma_{CC}(15a'), \left(10\,^1A'\leftarrow\widetilde{X}^1A'\right)$				
$3p'(4a'')^{-1}$	9.235	–	–	–
$13^1_0/4p(15a')^{-1}$	9.277	–	–	0.042
$13^2_0/4p(15a')^{-1}13^1_0$	9.329	–	–	0.052
$13^3_0/4p(15a')^{-1}13^2_0$	9.38(2)(s)	–	–	0.053
	$\overline{\Delta E}$	0.195	0.147	0.050

[a] (s) shoulder structure; (w) weak feature (the last decimal of the energy value is given in brackets for these less-resolved features);

performed with the EOM-CCSD method [25–28] and the aug-cc-pVTZ basis set (Table S2) as implemented in Psi4 [29].

Harmonic frequencies at the DFT/CAM-B3LYP/aug-cc-pVTZ level for the neutral and cationic electronic ground-states, and at the TD-DFT/CAM-B3LYP/aug-cc-pVTZ level for the first neutral electronic excited have been calculated (Tables S3–S5) and used to assign the major vibrational features within the valence, mixed valence-Rydberg and Rydberg excitations in the photoabsorption spectrum (Figs. 1–5).

Finally, we have obtained potential energy curves of the lowest-lying neutral excited states (TD-DFT/CAM-B3LYP/aug-cc-pVTZ) as a function of the C–C–C dihedral angle (Fig. 7) and C=O stretching mode (Fig. 8).

4. Structure and properties of β-propiolactone

The $CH_2CH_2CO_2$ molecule has C_S-symmetry in the electronic ground-state and the calculated outermost valence electronic configuration is $\widetilde{X}^1A'$ … $(12a')^2$ $(2a'')^2$ $(3a'')^2$ $(13a')^2$ $(14a')^2$ $(4a'')^2$ $(15a')^2$. A close inspection of the ground-state MOs in Fig. S4 shows for most of these a relevant electron density delocalized over the molecular frame, with contributions also from the C–O and the C–C bonds. The assignments are thus rather complex; however, we give the prevalent character of the molecular orbitals based on their visual inspection. The highest occupied molecular orbital (HOMO), 15a', is the O 2p lone pair orbital ($\overline{n}_O$) of the carbonyl group in the molecular plane with a contribution of σ_{CC}. The (HOMO-1), 4a'', is the endocyclic oxygen 2p orbital out-of-plane (n_O) whereas the (HOMO-2), 14a', is π_{CO}. The other MOs, (HOMO-3), 13a', (HOMO-4), 3a'', and (HOMO-5), 2a'', are $\overline{n}_O/\sigma_{CC}$, π_{CO} and π_{CO}, respectively.

The dominant VUV photoabsorption features shown in Figs. 1–5 have been assigned to electronic excitations from the (HOMO), (HOMO-1) and (HOMO-2) to valence, mixed valence-Rydberg and Rydberg character orbitals. The calculated excitation energies and oscillator strengths are in Table 1, while Table S1 includes a complete list of all transitions.

The fine structure in the β-propiolactone spectrum has been assigned to vibronic excitations, and the assignments are based on the information provided by the vibrational activation energies for the neutral electronic ground, neutral electronic first excited and cationic ground states. For the valence excitations, the fine structure has been assigned based on the energies (and wavenumbers) in the ground electronic state to 0.233 eV (1882 cm^{-1}) for C=O stretching, $\nu''_3(a')$, 0.164 eV (1319 cm^{-1}) for CH_2 wagging, $\nu''_6(a')$, 0.121 eV (978 cm^{-1}) for ring C–O stretching, $\nu''_{10}(a')$ and 0.064 eV (513 cm^{-1}) for C=O in-plane bending, $\nu''_{13}(a')$ (see Table S3 and [9]). These modes correspond to the calculated values in Table S4 to the neutral electronic first excited state 0.168 eV (1358 cm^{-1}) for C=O stretching, $\nu'_7(a)$, 0.165 eV (1332 cm^{-1}) for ring C–O stretching, $\nu'_{14}(a)$, 0.121 eV (978 cm^{-1}) for ring deformation, $\nu'_{13}(a)$, and 0.058 eV (468 cm^{-1}) for C=O bending, $\nu'_{19}(a)$, respectively.

The present threshold photoelectron spectrum shows the different ionic electronic states, from which the two lowest experimental ionisation energies at 10.560 eV $(15a')^{-1}$ (adiabatic) and 11.295 eV $\left(4a''\right)^{-1}$ (vertical) have been used to assign the different Rydberg orbitals based on their quantum defects. Moreover, the spectrum in Fig. 5 shows features that have been assigned in Table 5 to 0.195 eV (1572 cm^{-1}) for C=O stretching, $\nu'_3(a')$, 0.166 eV (1341 cm^{-1}) for CH_2 wagging, $\nu'_6(a')$,

Table 4
Proposed vibrational assignments of $CH_2CH_2CO_2$ absorption band in the photon energy range 9.4 – 10.8 eV[a]. Energies in eV. See text for details.

This work				
assignment	energy	$\Delta E(\nu'_3)$	$\Delta E(\nu'_6)$	$\Delta E(\nu'_{13})$
$4p'(15a')^{-1}$	9.411	–	–	–
$13^1_0/3d(4a'')^{-1}$	9.45(7)(b)	–	–	0.046
$\pi^*_{CO}(7a'')\leftarrow\pi_{CO}(14a') + \sigma^*_{CC}/4s(23a')\leftarrow\overline{n}_O/\sigma_{CC}(15a'), \left(16\,^1A'\leftarrow\tilde{X}^1A'\right)$				
0^0_0	9.53(0)(s)	–	–	–
13^1_0	9.58(5)(s)	–	–	0.055
13^2_0	9.62(6)(s)	–	–	0.041
6^1_0	9.69(5)(s)	–	0.165	–
$6^1_0 13^1_0$	9.740	–	–	0.045
$6^1_0 13^2_0$	9.789	–	–	0.049
$6^1_0 13^3_0$	9.840	–	–	0.051
3^1_0	9.718	0.188	–	–
$5s(15a')^{-1}/3d'(4a'')^{-1}/4s(4a'')^{-1}$	9.718	–	–	–
13^1_0	9.769	–	–	0.051
$\sigma^*_{CO}/3d''(22a') + \sigma^*_{CO}/3d'''(24a') + \sigma^*_{CO}/3d(25a')\leftarrow\overline{n}_O/\sigma_{CC}(15a'), \left(19\,^1A'\leftarrow\tilde{X}^1A'\right)$				
$5p'(15a')^{-1}$	9.893	–	–	–
13^1_0	9.94(3)(s)	–	–	0.050
6^1_0	10.054	–	0.161	–
$6s(15a')^{-1}$	10.021	–	–	–
13^1_0	10.065	–	–	0.044
13^2_0	10.113	–	–	0.048
$13^3_0/7s(15a')^{-1}/6d'(15a')^{-1}$	10.164	–	–	0.051
$13^4_0/7s(15a')^{-1}13^1_0/6d'(15a')^{-1}13^1_0$	10.213	–	–	0.049
$13^5_0/7d(15a')^{-1}/7s(15a')^{-1}13^2_0/6d'(15a')^{-1}13^2_0$	10.265	–	–	0.052
$10s(15a')^{-1}$	10.394	–	–	–
13^1_0	10.435	–	–	0.041
13^2_0	10.490	–	–	0.055
$5p(4a'')^{-1}$	10.554	–	–	–
13^1_0	10.602	–	–	0.048
	$\overline{\Delta E}$	0.188	0.163	0.048

[a](b) broad feature; (s) shoulder structure (the last decimal of the energy value is given in brackets for these less-resolved features).

0.107 eV (864 cm^{-1}) for ring C–O stretching, $\nu'_{10}(a')$, and 0.046 eV (368 cm^{-1}) for C=O in-plane bending, $\nu'_{13}(a')$ modes (see Table S5). Such information from the fine structure has been relevant to assign the main vibrational modes in the different Rydberg states.

5. Results and discussion

The absolute photoabsorption spectrum of β-propiolactone is shown in Fig. 1 in the energy range 4.0 to 10.8 eV, while expanded sections are plotted in Figs. 2–4. Although the spectra were measured down to an energy of 3.76 eV, no absorption features were found before the onset to the first band above 4.6 eV (Fig. 2). Early photoabsorption measurements have revealed some water contamination in particular in the 9.9–10.8 eV (115–225 nm) energy region where Rydberg excitation shows very narrow features [30]. This was mostly removed through repeated sample pumping and measurements until the water absorption features were not discernible in the spectrum. However, there the presence of some residual water may have an effect on β-propiolactone cross-sections, meaning that they may be underestimated by up to 5 %.

The dominant absorption bands are assigned to electronic excitations from the ground-state to valence, mixed valence-Rydberg and Rydberg states (Section 5.7), the latter converging to the ionic electronic ground state $(15a')^{-1}\ \tilde{X}^2A'$ and the ionic first electronic excited state $(4a'')^{-1}\ \tilde{A}^2A''$. The spectrum above 7.0 eV is rich in fine structure, with mostly the C=O stretching, $\nu'_3(a')$, the CH_2 wagging, $\nu'_6(a')$, and the C=O in-plane bending, $\nu'_{13}(a')$ modes being active; the structures are largely due to the overlap of different Rydberg transitions contributing to the absorption spectrum. Note that the absorption features are shifted from the spectrum baseline above ~ 7.5 eV which is partially due to the underlying dissociative character of the electronic transition to σ^*_{CC} and σ^*_{CO} antibonding molecular orbitals (Table 1).

Table 1 shows the TD-DFT calculation results for β-propiolactone together with the experimental data, and a good level of agreement is noted to within 6 %. The assignments of the different members associated with Rydberg series have not been labelled in Fig. 5 to avoid congestion, whereas the related values are listed in Table 6 and Tables 2–5 list the vibronic assignments superimposed on the Rydberg series.

The next sections deal with a detailed description of the VUV photoabsorption features in the different photon energy ranges with the analysis aided by our theoretical calculations (Tables 1, S1 and S2).

5.1. The 4.5–6.8 eV photon energy range

The calculations performed with the aug-cc-pVTZ basis set assign the lowest-lying valence transition to $\pi^*_{CO}(7a'')(57\%) + \pi^*_{CO}/3d'(6a'')(30\%)\leftarrow\overline{n}_O/\sigma_{CC}(15a'), \left(1^1A''\leftarrow\tilde{X}^1A'\right)$, with a cross-section of 0.16 Mb (Table 1). The vertical excitation energy value of 6.02(5)

Table 5
Energy positions and vibrational analyses of features in the lowest-lying threshold photoelectron bands of $CH_2CH_2CO_2$.

assignment	energy	$\Delta E(\nu'_3)$	$\Delta E(\nu'_6)$	$\Delta E(\nu'_{10})$	$\Delta E(\nu'_{13})$
$(15a')^{-1}, \left(\tilde{X}^2A' \leftarrow \tilde{X}^1A'\right)$					
0_0^0	10.560	–	–	–	–
13_0^1	10.608	–	–	–	0.048
13_0^2	10.657	–	–	–	0.049
6_0^1	10.72(3)(s)	–	0.163	–	–
3_0^1	10.758	0.198	–	–	–
$3_0^1 13_0^1$	10.807	–	–	–	0.049
$3_0^1 13_0^2$	10.860	–	–	–	0.053
6_0^2	10.87(8)(s)	–	0.155	–	–
$6_0^2 13_0^1$	10.93(0)(b)	–	–	–	0.052
3_0^2	10.95(6)(s)	0.198	–	–	–
$3_0^2 13_0^1$	11.001	–	–	–	0.045
$(4a'')^{-1}, \left(\tilde{A}^2A'' \leftarrow \tilde{X}^1A'\right)$					
0_0^0	11.12(3)(s,w)	–	–	–	–
6_0^1	11.29(5)(b)	–	0.172	–	–
6_0^2	11.46(7)(s,b)	–	0.172	–	–
	$\overline{\Delta E}$	0.198	0.166	–	0.049
$(3a'')^{-1}, \left(\tilde{D}^2A'' \leftarrow \tilde{X}^1A'\right)$					
0_0^0	16.124	–	–	–	–
10_0^1	16.215	–	–	0.091	–
3_0^1	16.296	0.172	–	–	–
$3_0^0 13_0^1$	16.35(1)(b)	–	–	–	0.055
$(2a'')^{-1}, \left(\tilde{E}^2A'' \leftarrow \tilde{X}^1A'\right)$					
0_0^0	16.74(8)(b)	–	–	–	–
10_0^1	16.82(9)(s)	–	–	0.081	–
3_0^1	16.92(6)(b,w)	0.178	–	–	–
$11_0^1 3_0^1$	17.00(9)(w)	0.180	–	–	–
3_0^2	17.08(2)(b,w)	0.156	–	–	–
$11_0^1 3_0^2$	17.17(8)(b,w)	0.169	–	–	–
	$\overline{\Delta E}$	0.171	–	0.086	0.055

[a](s) shoulder structure; (b) broad feature; (w) weak feature (the last decimal of the energy value is given in brackets for these less-resolved features).

eV is in good agreement with the calculated value 6.050 eV as shown in Table 1. This electronic transition indicates that $(6a'')$ is a combination of a valence π^*_{CO} and a Rydberg *d* orbital. However, given the broad and almost structureless nature of the photoabsorption band, one would expect it to be mostly valence in character, making the Rydberg contribution negligible. To further investigate the nature of the band, we performed additional calculations using the cc-pVTZ basis set while keeping the same functional. The exclusion of augmented functions purposefully hinders the description of Rydberg states. Therefore, if the nature of the band would contain any Rydberg contribution, we would expect it to be poorly described with the more compact cc-pVTZ basis set. However, the calculations show negligible differences between both basis sets, i.e., with the aug-cc-pVTZ the vertical excitation energy is at 6.050 eV with an oscillator strength $f_L = 0.000594$, whereas with the cc-pVTZ it is at 6.089 eV and $f_L = 0.000939$. Moreover, in the cc-pVTZ calculation, the state is predominantly described by a single transition, $(5a'') \leftarrow (15a')$(93%) (the ordering of molecular orbitals differs between basis sets). From the visual inspection of the $(5a'')$ orbital depicted in Fig. S5, it clearly exhibits a π* character while no Rydberg component is noted. Although the more diffuse basis set (aug-cc-pVTZ) suggests a minor Rydberg *d* contribution in one of the dominant transitions, we assign this band to a valence π* character only. It is important to note that augmented functions are also relevant to describe the remaining states in the photoabsorption spectrum.

Table 6
Energy values (eV), quantum defects (δ) and assignments of the Rydberg series converging to $(15a')^{-1}\ \tilde{X}^2A'$ and $(4a'')^{-1}\ \tilde{A}^2A''$ of β-propiolactone, $CH_2CH_2CO_2$. See text for details.

E_n	δ	assignment	E_n	δ	assignment
$(IE_1)_{ad}$ = 10.560 eV $(15a')^{-1}$			**$(IE_2)_v$ = 11.295 eV** $(4a'')^{-1}$		
$(ns \leftarrow 15a')$			$(ns \leftarrow 4a'')$		
7.234	0.98	3 s	7.89(0)(b)/ 7.989	1.00/ 0.97	3 s
9.020	1.03	4 s	9.718/9.766	1.02	4 s
9.718	0.98	5 s	10.438	1.06	5 s
10.021	0.98	6 s	–	–	–
10.164	1.14	7 s	–	–	–
–	–	8 s	–	–	–
10.356	0.83	9 s	–	–	–
10.394	0.95	10 s	–	–	–
$(np \leftarrow 15a')$			$(np \leftarrow 4a'')$		
7.89(0)(b)/ 7.989	0.70/ 0.74	3p	8.762	0.68	3p
9.277	0.74	4p	10.06(9)(b)	0.67	4p
9.839	0.66	5p	10.554	0.71	5p
10.092	0.61	6p	–	–	–
10.22(5)(s)	0.63	7p	–	–	–
$(np' \leftarrow 15a')$			$(np' \leftarrow 4a'')$		
8.307	0.54	3p'	9.235	0.43	3p'
9.411	0.56	4p'	10.22(5)(s)	0.43	4p'
9.893	0.48	5p'	10.659	0.7	5p'
10.113	0.48	6p'	–	–	–
–	–	7p'	–	–	–
10.315	0.55	8p'	–	–	–
10.368	0.58	9p'	–	–	–
$(nd \leftarrow 15a')$			$(nd \leftarrow 4a'')$		
8.707	0.29	3d	9.45(7)(b)	0.28	3d
9.61(1)(b)	0.21	4d	10.318	0.27	4d
9.963	0.22	5d	10.687	0.27	5d
–	–	6d	–	–	–
10.265	0.21	7d	–	–	–
10.334	0.24	8d	–	–	–
10.417	0.24	9d	–	–	–
$(nd' \leftarrow 15a')$			$(nd' \leftarrow 4a'')$		
8.907	0.13	3d'	9.718/9.766	0.03/ 0.02	3d'
9.63(7)(s)	0.16	4d'	10.417	0.06	4d'
9.983	0.14	5d'	–	–	–
10.164	0.14	6d'	–	–	–
10.26(9)(b)	0.16	7d'	–	–	–
10.337	0.18	8d'	–	–	–

[a](s) shoulder structure; (b) broad structure (the last decimal of the energy value is given in brackets for these less-resolved features).

We have also calculated at the EOM-CCSD level of theory a vertical excitation energy of 6.178 eV and an oscillator strength of $f_L \approx 0.00053$ (see Table S2). The oscillator strength is in good agreement with the TD-DFT calculation result albeit with a 3 % higher calculated energy than the experimental value.

A close inspection of Fig. 2 in the energy region 4.6–6.5 eV (268–190 nm) shows less smooth cross-section data with a low magnitude (< 0.17 Mb). Such weak absorption by the sample, where the intensity I_t becomes close to that of the transmitted light through the empty gas cell ($I_0 \approx I_t$), contributes to lower accuracy in the absolute values, because the error increases as a percentage of the measured cross-section. However, shoulders and weak features are noticeable and we tentatively assign the 0_0^0 origin band at 5.40(9) eV (Table 2). The weak fine structure shows a few quanta of ring C–O stretching, $\nu'_{10}(a')$ mode with an average spacing of 0.101 eV (815 cm^{-1}). Since we are not able to assign the origin of this vibrational mode, the notation 10^n was used. To further support this

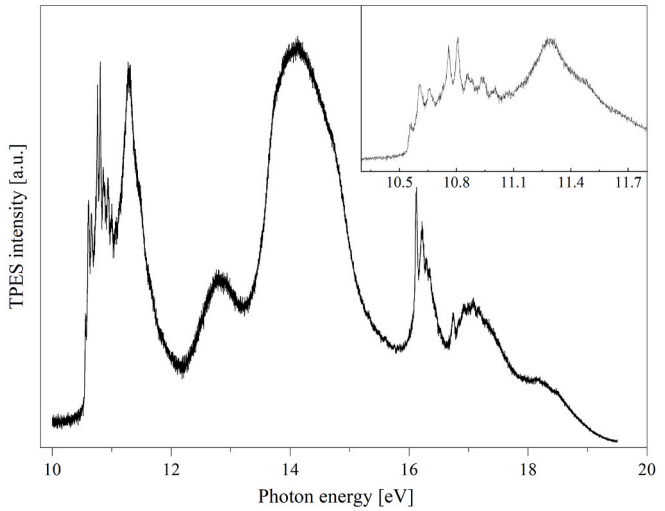

Fig. 6. Threshold photoelectron spectrum of CH_2 CH_2 CO_2 in the 10 – 20 eV region, collected at 80 eV initial photon energy. Inset with the expanded view of the lowest-lying ionic bands. See text for details.

assignment, we have obtained at the DFT and TD-DFT/CAM-B3LYP/aug-cc-pVTZ level the bond lengths in Å and bond angles in (°) for the neutral ground-state (Fig. S1) and neutral first excited-state (Fig. S2) molecular structures, respectively. An inspection of the two geometrical structures shows no relevant changes within the bond lengths and bond angles (< 2 %), except for the loss of planar symmetry. However, relevant shortening from the ground-state to the first excited-state of ~ 9 % is noted within the ∡ O1 – C2 – O3 angle. This change is consistent with the general ring C–O stretching related to $\nu'_{10}(a')$ mode.

5.2. The 6.8–9.4 eV photon energy range

The theoretical calculations within this energy range allow us to assign six electronic excitations with valence, mixed valence-Rydberg and Rydberg characters (Table 1). The first absorption band centred at 7.341 eV, is assigned to the $3s(16a')(71\%) + \sigma^*_{CC}/3\,p''(18a')(13\%) \leftarrow \bar{n}_O/\sigma_{CC}(15a'), (2\,^1A' \leftarrow \tilde{X}^1A')$ transition with a cross-section of 12.32 Mb. The character of the band is remarkably Rydberg (see Sec. 5.7) in nature although the rather broad shape of the 3 *s* member is due to a contribution from the σ^*_{CC} antibonding character. The oscillator strength value obtained at the EOM-CCSD level of theory (see Table S2) is also in good accord with the TD-DFT calculation result (Table 1), although with a 4 % higher calculated energy than the corresponding experimental value. The fine structure has been assigned to one quantum of C=O stretching, $\nu'_3(a')$ and up to three quanta of C=O in-plane bending, $\nu'_{13}(a')$ modes (Table 2). These are marked in Fig. 3, with 13^3_0 as a dashed line, since the corresponding feature appears in the spectrum with weaker intensity relative to the first two quanta of such mode excitation.

The band with a vertical excitation energy at 7.487 eV and a cross-section value of 14.82 Mb is assigned to the calculated electronic transition at 7.959 eV, with an oscillator strength $f_L \approx 0.02896$, $\sigma^*_{CC}/3p''(18a')(22\%) \leftarrow \bar{n}_O/\sigma_{CC}(15a') + (\pi^*_{CO}/3p(5a'')(15\%) + \pi^*_{CO}(7a'')(46\%) \leftarrow n_O(4a'')), (3\,^1A' \leftarrow \tilde{X}^1A')$ (Table 1). The absorption band 0^0_0 origin at 7.44 (2) eV contains vibrational features involving the C=O stretching, $\nu'_3(a')$ and the C=O in-plane bending, $\nu'_{13}(a')$ modes, with average excitation energies of 0.198 and 0.054 eV (Table 2).

The next electronic transition, with the 0^0_0 origin at 7.890 eV (a cross-section value of 11.73 Mb) is assigned to the mixed valence-Rydberg and Rydberg character $\pi^*_{CO}/3p(5a'')(23\%) \leftarrow n_O(4a'') + (3p'(17a')(23\%) + \sigma^*_{CC}/3p''(18a')(37\%)) \leftarrow \bar{n}_O/\sigma_{CC}(15a'), (5\,^1A' \leftarrow \tilde{X}^1A')$. From the calculated quantum defects the assignment of the Rydberg transition is discussed below. However, if we take the next absorption feature at 7.989 eV, this can also be assigned to a Rydberg transition, which has been marked in Fig. 3 as a dashed line. This band also shows a contribution of one quantum of C=O in-plane bending, $\nu'_{13}(a')$ mode (Sec. 5.7).

The electronic band with a peak at 8.316 eV (Fig. 3 and a cross-section value of 16.48 Mb), is assigned to the calculated electronic transition at 8.763 eV ($f_L \approx 0.05908$), $(\pi^*_{CO}/3p(5a'')(48\%) + \pi^*_{CO}/3d'(6a'')(15\%) + \pi^*_{CO}(7a'')(13\%) \leftarrow n_O(4a'')), (6\,^1A' \leftarrow \tilde{X}^1A')$ (Table 1). The absorption band shows one quantum of CH_2 wagging, $\nu'_6(a')$, and C=O in-plane bending, $\nu'_{13}(a')$ modes (Table 2) while the Rydberg character will be discussed in Sec. 5.7.

Fig. 4 shows two electronic transitions with vertical excitation energies at 8.907 and 9.277 eV with local cross-section values of 27.71 and 22.46 Mb, respectively, which have been assigned in Table 1 to $\sigma^*_{CO}/3d(20a')(57\%) + 3d'(21a')(21\%) \leftarrow \bar{n}_O/\sigma_{CC}(15a'), (7\,^1A' \leftarrow \tilde{X}^1A')$ and $\sigma^*_{CO}/3d(20a')(11\%) + 3d'(21a')(60\%) \leftarrow \bar{n}_O/\sigma_{CC}(15a'), (10\,^1A' \leftarrow \tilde{X}^1A')$, the former with prevalent mixed valence-Rydberg, the latter being mainly Rydberg in character (Sec. 5.7). A relevant background contribution to the spectrum is noted in Figs. 1 and 4, shifting the absorption features

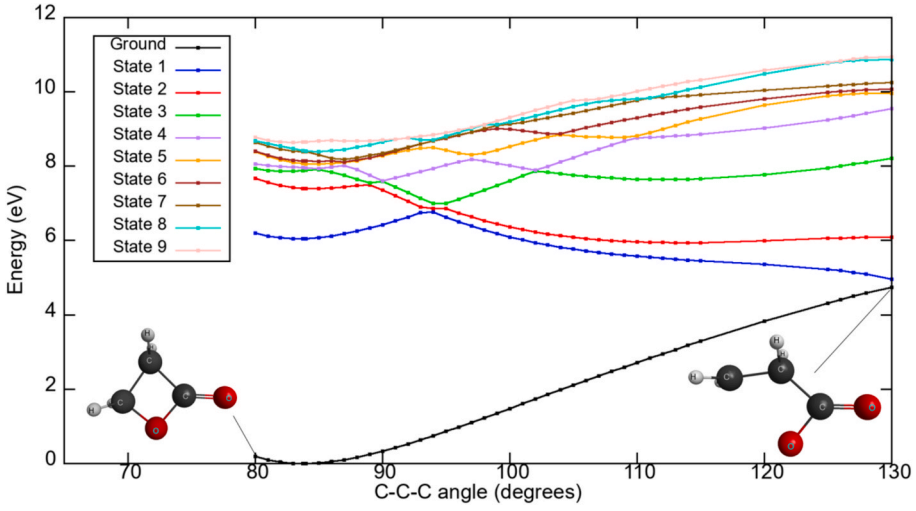

Fig. 7. PECs for the nine lowest-lying excited singlet states of CH_2 CH_2 CO_2 plotted as a function of the C–C–C dihedral angle (in degrees). The calculations were performed at the TD-DFT/CAM-B3LYP/aug-cc-pVTZ level of theory in the C_1 symmetry group. See text for details.

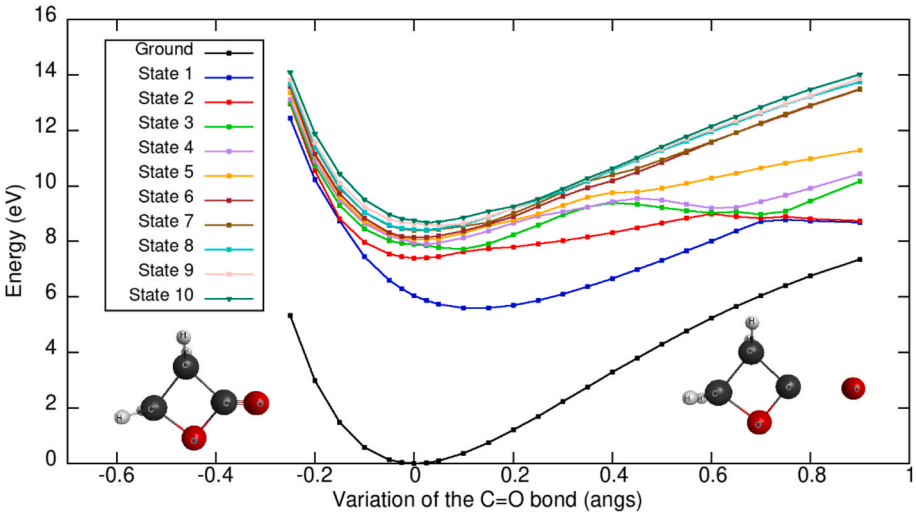

Fig. 8. PECs for the ten lowest-lying excited singlet states of CH_2 CH_2 CO_2 plotted as a function of the $R_{C=O}$ bond length (in Å). The calculations were performed at the TD-DFT/CAM-B3LYP/aug-cc-pVTZ level of theory in the C_1 symmetry group. See text for details.

from the baseline, which is due to the underlying dissociative character of the σ^*_{CO} antibonding molecular orbital. The $(7\,^1A' \leftarrow \tilde{X}^1A')$ electronic excitation is accompanied by quite extensive vibrational fine structure with assignments in Table 3, rendering the pre-dissociative nature of the transition. The main vibrational mode is assigned to C=O in-plane bending, $\nu'_{13}(a')$, although with combinations of the CH_2 wagging, $\nu'_6(a')$ and the C=O stretching, $\nu'_3(a')$ modes. The high number of quanta related to 13^n_0 (n = 1–11) may seem implausible for a pre-dissociative transition, however four quanta of the C=O in-plane bending, $\nu'_{13}(a')$ mode can also be assigned to the contribution of $3d'(15a')^{-1}$, meaning that the feature at 8.952 eV can also be assigned to $3d'(15a')^{-1}3^1_0$ instead (Table 3).

5.3. The 8.7–10.8 eV photon energy range

The absorption features in this photon energy region are classified as valence and mixed valence-Rydberg (Sec. 5.7). An expanded plot of the measured photoabsorption spectrum is shown in Fig. 5, with the proposed assignments summarised in Table 4. Of relevance are the shapes of some features, which appear superimposed either on the vibrational fine structure or on the Rydberg series, resulting in broadening the shape of those peaks. The two most relevant electronic states have 0^0_0 transitions at 9.53(0) and 9.893 eV, with cross-sections of 32.95 and 38.76 Mb at their vertical values of 9.764 and 10.394 eV. From the calculations in Table 1, these features have been assigned to the $3p'(17a')(53\%) \leftarrow \pi_{CO}(14a') + \sigma^*_{CC}/\ 4s(23a')(15\%) \leftarrow \bar{n}_O/\sigma_{CC}(15a')$, $(16\,^1A' \leftarrow \tilde{X}^1A')$ and the $\sigma^*_{CO}/3d''(22a')(13\%) + \sigma^*_{CO}/3d''' \quad (24a')(14\%) + \sigma^*_{CO}/3d(25a')(18\%) \leftarrow \bar{n}_O/\sigma_{CC}(15a')$, $(19\,^1A' \leftarrow \tilde{X}^1A')$ transitions, with oscillator strengths $f_L \approx 0.06427$ and $f_L \approx 0.04670$, and show relevant fine structure superimposed on an underlying absorption continuum that may be assigned to pre-dissociation. The transitions are accompanied by 13^n_0 progressions (for the former, n = 1–3; for the latter, n = 1) from the C=O in-plane bending, $\nu'_{13}(a')$ mode, with an average energy spacing of 0.049 eV (395 cm^{-1}), together with contributions from the CH_2 wagging, $\nu'_6(a')$, mode (Table 4), with average spacings of 0.163 eV (1315 cm^{-1}). The energy values for $\nu'_{13}(a')$ are lower by 21 % than the ground-state energy (Table S3), providing evidence of shortening of the C=O bond and possible general ring deformation.

The photoabsorption spectrum in this energy range includes features due to the contribution of several members of the different Rydberg series converging to the ionic electronic ground $(15a')^{-1}\ \tilde{X}^2A'$ and first $(4a'')^{-1}\ \tilde{A}^2A''$ excited states of β-propiolactone and associated vibronic structure (Section 5.7).

5.4. Absolute photoabsorption cross sections and atmospheric photolysis

A thorough literature survey reveals no previous absolute ultra-violet photoabsorption studies of β-propiolactone in the wavelength range 268–115 nm (4.626–10.781 eV) to compare with the present data.

We have assessed the atmospheric photolysis of $CH_2CH_2CO_2$ from 0 km altitude (sea level) up to 50 km the limit of stratopause, using the present VUV absolute photoabsorption cross sections and the NASA solar actinic flux data [31]. For a comprehensive description of the methodology, see [32] and references therein. The quantum yield for dissociation is assumed to be 1.0 since no data is available in the literature. However, photodissociation data from experimental methods are needed to give an accurate value of such yield. The solar radiation reaching the Earth's atmosphere from 0 up to km altitude has wavelengths > 180 nm. The β-propiolactone cross-sections above 180 nm, have magnitudes < 1 Mb, thus meaning photolysis lifetimes of less than 10 sunlit days above 30 km. However, at altitudes lower than 25 km the photolysis lifetimes are high (> 100 sunlit days). According to Peyster [2], the degradation slow rate reaction of gas-phase β-propiolactone with $^{\bullet}OH$ radicals has an estimated half-life of 45 days. As far as the authors are aware, no detailed information on the rate coefficients for such reactions, and/or with any other atmospheric relevant radical species, is available in the literature that may provide a main sink mechanism in the troposphere. UV photolysis may therefore be a key removal process of any β-propiolactone in the stratosphere.

5.5. Ring strain integrity and potential energy curves along the C–O/C=O coordinates

The nature of the nuclear dynamics in the energy regions where relevant geometry changes may dictate the dissociative character of the electronic transitions, gives information on the rather intricate ring strain cohesion. Such geometrical modifications as well as vibrational excitations have been investigated from the calculated potential energy curves at the TD-DFT/CAMB3LYP/aug-cc-pVTZ level of theory in the C_1 symmetry group.

The nine lowest-lying excited states as a function of the C–C–C angle are shown in Fig. 7, with important avoided crossings observed for all states. Upon electronic excitation from the ground- to the first excited-state, C–O bond excision is only operative if the C–C–C angle increases

from its equilibrium geometry of ~ 85° up to ~ 95°. This seems implausible because the major contribution to the absorption band has been assigned to valence and mixed valence-Rydberg $\pi^*_{CO}(7a'') + \pi^*_{CO}/3d'(6a'') \leftarrow \overline{n}_O/\sigma_{CC}(15a')$ with π^*_{CO} character, which in principle will not lead to dissociation, unless a π^*_{CO}/σ^*_{CO} coupling occurs. This is only possible at higher energies, where the diabatic character of the states allow C–O dissociation above 95°, as long as the nuclear wave packet survives long enough to reach the asymptotic limits either from "state 1" or "state 2". We find no evidence of CO_2 formation which agrees with Noels *et al.* [8] study of the relative thermal stabilities of substituted β-lactones.

The higher energy states (labelled in Fig. 7) are in some cases almost degenerate at the equilibrium geometry (e.g. "states 5 and 6" and "states 7 and 8"), so any small increase in the C–C–C angle while the relevant adiabatic character of the potential energy curves is preserved, the electronic excited states can evolve along the repulsive character yielding dissociation only through states "1 and 2". This is only possible if the 95° C–C–C angle is surpassed.

We have also investigated the C=O bond dissociative character, while keeping all other atoms frozen. Fig. 8 shows the PECs for the ten lowest-lying excited states. The asymptotic limit can only be reached from electronic excitations to high energy states above 8 eV ("states 3–10"), meaning important changes between close lying electronic states as noted by the avoided crossings. Accessing these states can also yield bond excision with an oxygen atom being released from the carboxyl group, if a barrier is overcome (in "state 3").

5.6. Photoelectron spectrum

The photoelectron spectrum of β-propiolactone has been reported before [11,12] however with lower resolution than the present experiment (Fig. 6). From the shape of the lowest ionic band the adiabatic value is determined to be 10.560 eV, while the maximum intensity at 10.807 eV corresponds to the vertical ionisation energy (Table 5). The latter was previously reported at 10.78 and 10.7 eV [11,12]. The first band, corresponding to the ionisation of a lone-pair orbital $\overline{n}_O/\sigma_{CC}(15a')^{-1}$ within the carbonyl oxygen, shows fine structure which is assigned to C=O stretching, $\nu_3(a')$, CH_2 wagging, $\nu_6(a')$ and C=O in-plane bending, $\nu_{13}(a')$ modes from the calculated vibrational energies for the cationic electronic ground-state in Table S5. These modes show mean energies of 0.198, 0.166 and 0.049 eV, respectively (Table 5).

The second band in the spectrum refers to ionisation of the endocyclic oxygen lone-pair $n_O(4a'')^{-1}$ with a vertical value of 11.29(5) eV. The weak fine structure in this energy band is proposed to be mainly due to activation of the CH_2 wagging, $\nu_6(a')$ mode with mean energy of 0.172 eV (Table 5). The other ionic bands show vertical values at 12.757, 16.124 and 17.082 eV and are due to an electron being removed from $\pi_{CO}(14a')^{-1}$, $\overline{n}_O/\sigma_{CC}(13a')^{-1}$ and $\pi_{CO}(3a'')^{-1}$, respectively. The two higher energy bands show some fine structure, which is assigned in Table 5 to C=O stretching, $\nu_3(a')$, ring deformation, $\nu_{11}(a')$ and C=O in-plane bending, $\nu_{13}(a')$ modes, with mean energies of 0.171, 0.086 and 0.055 eV.

The optimised geometry of the $\tilde{X}^2A'$ ion with bond lengths in Å and bond angles in (°) is shown in Fig. S3. The major changes in the ionic state with respect to the ground state involve a decrease of 7 % in the O1–C2/O3–C2 and an increase of 4 % in the O1–C7 bond lengths, while ∡ O1–C2–O3 increases by 8 % (see Fig. S3 for atoms key). Thus, the most significant vibration features in the threshold photoelectron band involve these changes, which are in good agreement with the experimental values found.

5.7. Rydberg transitions

The photoabsorption spectrum above 7.0 eV exhibits features that have been assigned to different Rydberg transitions, along with fine structure (Figs. 3–5). These Rydberg states converge to $(15a')^{-1}\ \tilde{X}^2A'$ and $(4a'')^{-1}\ \tilde{A}^2A''$ ionic electronic states of $CH_2CH_2CO_2$ and have been assigned in Table 6 according to their positions and the quantum defects obtained from the Rydberg formula: $E_n = IE - R/(n-\delta)^2$, where *IE* is the ionisation energy of a given MO, *n* is the principal quantum number of the Rydberg orbital of energy E_n, *R* is the Rydberg constant (13.61 eV), and δ is the quantum defect resulting from the penetration of the Rydberg orbital into the core. We note in some energy ranges an overlap of different absorption features (Rydberg and vibrational modes) which contribute to relevant broadening and intensity enhancement of these features, e.g. the Rydberg members $10s(15a')^{-1}$, $3p(15a')^{-1}$ and $3s(4a'')^{-1}$ (see Table 6).

The lowest-lying Rydberg transition ($n = 3$) converging to the ionic electronic ground-state is assigned to the $(3s \leftarrow 15a')$ excitation, with the first member at 7.234 eV having a quantum defect $\delta = 0.98$. Higher-order Rydberg members of the *ns* series up to $n = 10$ are reported in Table 6. The $n = 7$ member has a quantum defect which is slightly larger than is typically expected for a *ns* series, and this is attributed to the contribution of the mixed valence-Rydberg character of the $\left(10\,^1A' \leftarrow \tilde{X}^1A'\right)$ transition (Sec. 5.3). The first members of the two n*p* $(np \leftarrow 15a')$ and $(np' \leftarrow 15a')$ series have absorption features at 7.89(0)/7.989 eV and 8.307 eV (δ = 0.70/0.74 and 0.54). In Table 6 we also include two n*d* $(nd \leftarrow 15a')$ and $(nd' \leftarrow 15a')$ series with principal quantum numbers up to $n = 9$, where $n = 3$ have been assigned at 8.707 and 8.907 eV ($\delta = 0.29$ and 0.13). The features at 9.718, 10.164, 10.22(5) and 10.417 eV can also be assigned to $4s(4a'')^{-1}/3d'(4a'')^{-1}$, $6d'(15a')^{-1}$, $4p'(4a'')^{-1}$ and $4d'(4a'')^{-1}$.

The Rydberg series converging to the ionic electronic fourth excited state IE_2, $(4a'')^{-1}$, are listed in Table 6, and have been assigned to the $(ns, np, np', nd, nd' \leftarrow 4a'')$ transitions. The first members of these series ($n = 3$) are associated with features at 7.89(0)/7.989 eV (δ = 1.00/0.97), 8.762 eV (δ = 0.68), 9.235 eV (δ = 0.43), 9.45(7) eV (δ = 0.28) and 9.718/9.766 eV (δ = 0.03/0.02), respectively (Table 6). Assignments for higher lying members up to $n = 5$ have been performed, while no attempt has been made above these quantum numbers because they lie outside the photon energy range investigated. The feature at 9.766 eV, $4s(4a'')^{-1}$, can also be assigned to $3d'(4a'')^{-1}$.

The absorption spectrum assigned to Rydberg excitations also shows fine structure from the different vibronic transitions (Tables 2–5). We make use of the information obtained from the present threshold photoelectron data on the vibrational frequencies for the (1 ^{2}A′) and (1 ^{2}A″) states of β-propiolactone cation to assign features to vibrational excitations. Moreover, we have obtained at the DFT/CAM-B3LYP/aug-cc-pVTZ level the bond lengths in Å and bond angles in (°) for the neutral ground-state (Fig. S1) and the cationic ground-state (Fig. S3). A close comparison between the two molecular structures shows that, upon ionisation, minor changes (< 3 %) are noted within the bond lengths (and bond angles) with exception of a ~ 8 % decrease in O1 – C2 and O3 – C2. These changes are related to variations in geometry in the cationic state involving the C–O and C=O modes while also affecting other modes within the ring structure. Table 5 lists the most relevant contributions from the C=O stretching, $\nu_3(a')$, CH_2 wagging, $\nu_6(a')$ and C=O in-plane bending, $\nu_{13}(a')$ modes in the $\tilde{X}^2A'$ cation ground-state, with average frequency values of 1597 cm^{-1} (0.198 eV), 1282 cm^{-1} (0.159 eV) and 395 cm^{-1} (0.049 eV), lower than the related values in the $\tilde{X}^1A'$ neutral ground state (Table S3), 1944 cm^{-1} (0.241 eV), 1364 cm^{-1} (0.169 eV) and 503 cm^{-1} (0.062 eV), respectively.

A close inspection of Tables 2–4 for the vibronic assignments of the Rydberg series converging to the ionic electronic ground $(15a')^{-1}\ \tilde{X}^2A'$

and first excited state $(4a'')^{-1}\ \tilde{A}^2A''$, shows that ν'_3, ν'_6 and ν'_{13} have average frequencies of 1565 cm^{-1} (0.194 eV) (1572 cm^{-1} in $\tilde{X}^2A'$, Table S6), 1242 cm^{-1} (0.154 eV) (1341 cm^{-1} in $\tilde{X}^2A'$, Table S6) and 411 cm^{-1} (0.051 eV) (368 cm^{-1} in $\tilde{X}^2A'$, Table S5). These changes are due to differences noted in the geometries of the ionic states relative to the neutral ground-state.

6. Conclusions

We have obtained for the first time a high-resolution photoabsorption spectrum of β-propiolactone in the photon energy range 4.6–10.8 eV (268–115 nm). Theoretical calculations at the DFT and TD-DFT levels with CAM-B3LYP functional and aug-cc-pVTZ basis set have been used to obtain vertical excitation energies and oscillator strengths of the valence, mixed valence-Rydberg and Rydberg transitions. Relevant information on the neutral ground-state, neutral first excited state and cationic ground-state geometries are also reported. The joint experimental and theoretical methodology employed constitutes the most accurate and up to date analysis of the electronic state spectroscopy of $CH_2CH_2CO_2$.

We have also obtained a high-resolution threshold photoelectron spectrum of β-butyrolactone from 10.4 to 19.4 eV and determined a new value of adiabatic ionisation energy of the ground ionic state at (10.560 ± 0.002) eV. The fine structure observed in both the absorption and threshold photoelectron spectra have been assigned to C=O stretching, $\nu'_3(a')$, CH_2 wagging, $\nu'_6(a')$, ring C–O stretching, $\nu'_{10}(a')$, and C=O in-plane bending, $\nu'_{13}(a')$ modes. The absolute photoabsorption cross-sections have also been used to derive photolysis rates in the terrestrial atmosphere from the surface up to the limit of the stratosphere, indicating that solar photolysis is expected to be a key sink for β-propiolactone at altitudes higher than 30 km. Potential energy curves for the lowest-lying excited states, were calculated at the TD-DFT level of theory with CAM-B3LYP functional and the aug-cc-pVTZ basis set. The results of the calculations provide new insights into the excited state dynamics as the reaction coordinates are changed. Relevant assessment of β-propiolactone ring strain integrity is also evaluated showing its fragile nature upon electronic excitation from the ground-state.

CRediT authorship contribution statement

P.A.S. Randi: Writing – original draft, Software, Investigation, Data curation. **M.H.F. Bettega:** Writing – review & editing, Writing – original draft, Supervision, Software, Resources, Investigation, Funding acquisition, Formal analysis, Data curation. **N.C. Jones:** Writing – review & editing, Validation, Supervision, Resources, Methodology, Investigation, Formal analysis, Data curation, Conceptualization. **S.V. Hoffmann:** Writing – review & editing, Visualization, Validation, Supervision, Resources, Project administration, Investigation, Funding acquisition, Formal analysis. **L. Zuin:** Writing – review & editing, Validation, Supervision, Methodology, Investigation. **M. Macdonald:** Validation, Supervision, Methodology, Investigation, Funding acquisition. **N.J. Mason:** Writing – review & editing, Validation, Resources, Project administration, Methodology, Data curation. **M.A. Śmiałek:** Writing – review & editing, Writing – original draft, Validation, Methodology, Investigation, Formal analysis, Data curation, Conceptualization. **P. Limão-Vieira:** Writing – review & editing, Writing – original draft, Supervision, Methodology, Formal analysis, Data curation, Conceptualization.

Declaration of competing interest

The authors declare that they have no known competing financial interests or personal relationships that could have appeared to influence the work reported in this paper.

Acknowledgments

PASR and MHFB acknowledge support from the Brazilian agencies Coordenação de Aperfeiçoamento de Pessoal de Nível Superior (CAPES) and Conselho Nacional de Desenvolvimento Científico e Tecnológico (CNPq). PASR and MHFB also acknowledge Prof. Carlos de Carvalho for computational support at LFTC-DFis-UFPR and at LCPAD-UFPR. The authors wish to acknowledge the beam time at the ISA synchrotron, Aarhus University, Denmark. The research leading to this result has been co-funded by the project NEPHEWS under Grant Agreement No 101131414 from the EU Framework Programme for Research and Innovation Horizon Europe. PLV acknowledges the Portuguese National Funding Agency (FCT) through research grant CEFITEC (UIDB/00068/2020), as well as his visiting professor position at Federal University of Paraná, Curitiba, Brazil. Research described in this paper was performed at the Canadian Light Source, which is supported by the Natural Sciences and Engineering Research Council of Canada, the National Research Council Canada, the Canadian Institutes of Health Research, the Province of Saskatchewan, Western Economic Diversification Canada, and the University of Saskatchewan.

Appendix A. Supplementary data

Supplementary data to this article can be found online at https://doi.org/10.1016/j.jphotochem.2025.116573.

Data availability

Data will be made available on request.

References

[1] E. Španinger, U. Bren, Carcinogenesis of β-Propiolactone: A Computational Study, Chem. Res. Toxicol. 33 (2020) 769–781, https://doi.org/10.1021/acs.chemrestox.9b00389.
[2] A. Peyster, Beta-Propiolactone, in: Encyclopedia of Toxicology: Third Edition, Elsevier, 2014: pp. 442–445. https://doi.org/10.1016/B978-0-12-386454-3.01168-4.
[3] B. Jollès, L. Chinsky, A. Laigle, UV resonance Raman study of the DNA–β-propiolactone interaction, J. Raman Spectrosc. 19 (1988) 155–159, https://doi.org/10.1002/jrs.1250190303.
[4] K. Hemminki, Reactions of β-propiolactone, β-butyrolactone and gamma-butyrolactone with nucleic acids, Chem. Biol. Interactions 34 (1981) 323–331.
[5] Z. Chen, J. van Wijngaarden, A combined ab initio, Fourier transform microwave and Fourier transform infrared spectroscopic investigation of β-propiolactone: The ν8 and ν12 bands, J. Mol. Spectrosc. 257 (2009) 164–169, https://doi.org/10.1016/j.jms.2009.08.007.
[6] Y. Sasaki, N. Yoshino, S. Sato, Y. Muraki, Analysis of the beta-propiolactone sensitivity and optimization of inactivation methods for human influenza H3N2 virus, J. Virol. Methods 235 (2016) 105–111, https://doi.org/10.1016/j.jviromet.2016.04.013.
[7] S. Lei, X. Gao, Y. Sun, X. Yu, L. Zhao, Gas chromatography-mass spectrometry method for determination of β-propiolactone in human inactivated rabies vaccine and its hydrolysis analysis, J. Pharm. Anal. 8 (2018) 373–377, https://doi.org/10.1016/j.jpha.2018.06.003.
[8] A.F. Noels, J.J. Herman, P. Teyssié, J.M. André, J. Delhalle, J.G. Fripiat, The electronic structure of β-propiolactone (2-oxetanone) and some 3- and 4-substituted 2-oxetanones, J. Mol. Struct. THEOCHEM 109 (1984) 293–303.
[9] J.R. Durig, Far-infrared absorption, vibrational spectra and structure of beta-propiolactone, Spectrochim. Acta 19 (1963) 1225–1233.
[10] K.J. Jakanent, P.J. Stephens, Ab Inltlo Calculatlon of Force Fields and Vibrational Spectra: 2-Oxetanone, J. Phys. Chem 95 (1991) 5446–5454.
[11] M. Jinno, I. Watanabe, S.I. Yokoyama, He I Photoelectron Spectra of Ethylene Carbonate and Related Compounds, Bull. Chem. Soc. Jap. 50 (1977) 597–603.
[12] P.C. Martino, P. Shevlin, S.D. Worley, The electronic structures of small strained rings. An investigation of the interaction between the oxygen and the π orbitals in 3-methyleneoxetane and 3-oxetanone, Chem. Phys. Lett. 68 (1979) 237–241.
[13] K. Watanabe, T. Nakayama, J. Mottl, Ionization Potentials of Some Molecules, J. Quant. Spectrosc. Radiat. Transfer 2 (1962) 369–382.
[14] S. Eden, P. Limão-Vieira, S.V. Hoffmann, N.J. Mason, VUV photoabsorption in CF3X (X = Cl, Br, I) fluoro-alkanes, Chem. Phys. 323 (2006) 313–333.
[15] M.H. Palmer, T. Ridley, S.V. Hoffmann, N.C. Jones, M. Coreno, M. De Simone, C. Grazioli, M. Biczysko, A. Baiardi, P. Limão-Vieira, Interpretation of the vacuum

ultraviolet photoabsorption spectrum of iodobenzene by ab initio computations, J. Chem. Phys. 142 (2015) 134302.
[16] Y.F. Hu, L. Zuin, G. Wright, R. Igarashi, M. McKibben, T. Wilson, S.Y. Chen, T. Johnson, D. Maxwell, B.W. Yates, T.K. Sham, R. Reininger, Commissioning and performance of the variable line spacing plane grating monochromator beamline at the Canadian Light Source, Rev. Sci. Instrum. 78 (2007), https://doi.org/10.1063/1.2778613.
[17] T.J. Reddish, G. Richmond, G.W. Bagley, J.P. Wightman, S. Cvejanovic, Dual toroidal photoelectron spectrometer for investigating photodouble ionization in atoms and molecules, Rev. Sci. Instrum. 68 (1997) 2685–2692, https://doi.org/10.1063/1.1148180.
[18] M.A. Śmiałek, M.A. MacDonald, S. Ptasińska, L. Zuin, N.J. Mason, Photoelectron and threshold photoelectron valence spectra of pyridine, Eur. Phys. J. D 70 (2016) 42, https://doi.org/10.1140/epjd/e2016-60673-0.
[19] K.P. Huber, C. Jungen, High-resolution jet absorption study of nitrogen near 800 Å, J. Chem. Phys. 92 (1990) 850–861, https://doi.org/10.1063/1.458589.
[20] D.A. Shaw, D.M.P. Holland, M.A. Macdonald, A. Hopkirk, M.A. Hayes, S. M. Mcsweeney, A study of the absolute photoabsorption cross section and the photoionization quantum efficiency of nitrogen from the ionization threshold to 485 A, Chem. Phys. 166 (1992) 379–391.
[21] T. Yanai, D.P. Tew, N.C. Handy, A new hybrid exchange-correlation functional using the Coulomb-attenuating method (CAM-B3LYP), Chem. Phys. Lett. 393 (2004) 51–57.
[22] G.M.J. Barca, C. Bertoni, L. Carrington, D. Datta, N. De Silva, J.E. Deustua, D. G. Fedorov, J.R. Gour, A.O. Gunina, E. Guidez, T. Harville, S. Irle, J. Ivanic, K. Kowalski, S.S. Leang, H. Li, W. Li, J.J. Lutz, I. Magoulas, J. Mato, V. Mironov, H. Nakata, B.Q. Pham, P. Piecuch, D. Poole, S.R. Pruitt, A.P. Rendell, L.B. Roskop, K. Ruedenberg, T. Sattasathuchana, M.W. Schmidt, J. Shen, L. Slipchenko, M. Sosonkina, V. Sundriyal, A. Tiwari, J.L. Galvez Vallejo, B. Westheimer, M. Włoch, P. Xu, F. Zahariev, M.S. Gordon, Recent developments in the general atomic and molecular electronic structure system, J. Chem. Phys. 152 (2020) 154102.
[23] R. Bauernschmitt, R. Ahlrichs, Treatment of electronic excitations within the adiabatic approximation of time dependent density functional theory, Chem. Phys. Lett. 256 (1996) 454–464.
[24] M.E. Casida, Time-dependent density-functional theory for molecules and molecular solids, J. Mol. Struct.-Theochem 914 (2009) 3–18.
[25] K. Emrich, An extension of the coupled cluster formalism to excited states (I), Nucl. Phys. A 351 (1981) 379–396.
[26] H. Sekino, R.J. Bartlett, A linear response, coupled-cluster theory for excitation energy, Int. J. Quantum Chem. 26 (1984) 255–265.
[27] J.F. Stanton, R.J. Bartlett, The equation of motion coupled-cluster method. A systematic biorthogonal approach to molecular excitation energies, transition probabilities, and excited state properties, J. Chem. Phys. 98 (1993) 7029–7039.
[28] R.J. Bartlett, Coupled-cluster theory and its equation-of-motion extensions, Wiley Interdiscip. Rev. Comput. Mol. Sci. 2 (2012) 126–138.
[29] R.M. Parrish, L.A. Burns, D.G.A. Smith, A.C. Simmonett, A.E. DePrince, E. G. Hohenstein, U. Bozkaya, A.Y. Sokolov, R. Di Remigio, R.M. Richard, J. F. Gonthier, A.M. James, H.R. McAlexander, A. Kumar, M. Saitow, X. Wang, B. P. Pritchard, P. Verma, H.F. Schaefer, K. Patkowski, R.A. King, E.F. Valeev, F. A. Evangelista, J.M. Turney, T.D. Crawford, C.D. Sherrill, Psi4 1.1: An Open-Source Electronic Structure Program Emphasizing Automation, Advanced Libraries, and Interoperability, J. Chem. Theory Comput. 13 (2017) 3185–3197.
[30] R. Mota, R. Parafita, A. Giuliani, M.-J. Hubin-Franskin, J.M.C. Lourenço, G. Garcia, S.V. Hoffmann, N.J. Mason, P.A. Ribeiro, M. Raposo, P. Limão-Vieira, Water VUV electronic state spectroscopy by synchrotron radiation, Chem. Phys. Lett. 416 (2005) 152–159.
[31] Chemical Kinetics and Photochemical Data for Use in Stratospheric Modelling, Evaluation number 12, NASA, Jet Propulsion Laboratory, JPL, Publication 97-4, January 15, 1997.
[32] P. Limão Vieira, S. Eden, P.A. Kendall, N.J. Mason, S.V. Hoffmann, VUV photo-absorption cross-section for CCl<inf>2</inf>F<inf>2</inf>, Chem Phys Lett 364 (2002), https://doi.org/10.1016/S0009-2614(02)01304-0.